Perovskite Oxide Catalysts for Enhanced CO₂ Reduction: Embroidering Surface Decoration with Ni and Cu Nanoparticles

Andrea Osti [1] , Lorenzo Rizzato [1], Jonathan Cavazzani [1,*] , Ambra Meneghello [1] and Antonella Glisenti [1,2,*]

1 Department of Chemical Sciences, University of Padova, Via F. Marzolo, 1, 35131 Padova, Italy; andrea.osti.1@phd.unipd.it (A.O.); lorenzo.rizzato.1@phd.unipd.it (L.R.); ambra.meneghello@studenti.unipd.it (A.M.)
2 CNR-ICMATE, INSTM, Via F. Marzolo, 1, 35131 Padova, Italy
* Correspondence: jonathan.cavazzani@phd.unipd.it (J.C.); antonella.glisenti@unipd.it (A.G.)

Abstract: The imperative reduction of carbon dioxide into valuable fuels stands as a crucial step in the transition towards a more sustainable energy system. Perovskite oxides, with their high compositional and property adjustability, emerge as promising catalysts for this purpose, whether employed independently or as a supporting matrix for other active metals. In this study, an A-site-deficient $La_{0.9}FeO_3$ perovskite underwent surface decoration with Ni, Cu or Ni + Cu via a citric acid-templated wet impregnation method. Following extensive characterization through XRD, N_2 physisorption, H_2-TPR, SEM-EDX, HAADF STEM-EDX mapping, CO_2-TPD and XPS, the prepared powders underwent reduction under diluted H_2 to yield metallic nanoparticles (NPs). The prepared catalysts were then evaluated for CO_2 reduction in a $CO_2/H_2 = 1/4$ mixture. The deposition of Ni or Cu NPs on the perovskite support significantly enhanced the conversion of CO_2, achieving a 50% conversion rate at 500 °C, albeit resulting in only CO as the final product. Notably, the catalyst featuring Ni-Cu co-deposition outperformed in the intermediate temperature range, exhibiting high selectivity for CH_4 production around 350 °C. For this latter catalyst, a synergistic effect of the metal–support interaction was evidenced by H_2-TPR and CO_2-TPD experiments as well as a better nanoparticle dispersion. A remarkable stability in a 20 h time-span was also demonstrated for all catalysts, especially the one with Ni-Cu co-deposition.

Keywords: CO_2 reduction; $LaFeO_3$ perovskite; Ni and Cu metals; templated impregnation

1. Introduction

According to the Intergovernmental Panel on Climate Change (IPCC), 2400 ± 240 $GtCO_2$ were emitted into the atmosphere by anthropogenic activities, causing the global surface temperature to increase and therefore rapid changes in the Earth's equilibrium [1]. Extreme climate phenomena are observed throughout the entire planet, damaging local ecosystems and endangering human societies [2]. As a greenhouse gas (GHG), high carbon dioxide concentrations lead to exponential temperature positive variations with time [3]; thus, finding new ways to promote a cost-effective, easy and scalable CO_2 concentration decrease is crucial to ensure a sustainable future for humankind [4]. As a stable molecule, carbon dioxide is difficult to activate and convert to valuable products such as syngas or methane [5]; poor adsorption on various catalysts and the difficult C-O double bond cleavage are some of the bottlenecks for obtaining high yields and selectivity in the CO_2 reduction reaction (CO_2RR) [6,7]. The first attempt to valorize carbon dioxide was made by F. W. Hightower et al., studying the production of methane from a CO_2-containing mixture via water gas shift [8]; from that moment, different ways to use carbon dioxide have been tested, from thermal-activated processes to bio-based reactions [9–11].

In this regard, perovskite and perovskite-based systems are good candidates as the next generation of materials [12]; their compositional flexibility allows us to obtain a broad

spectrum of materials [13], from ferroelectric structures to visible light absorbers [14,15]. Particularly, perovskite-based systems are widely exploited as catalysts, for their good thermal and chemical stability in different environments [16]. As mentioned above, perovskitic structures can be designed to obtain suitable properties based on the particular case study; among different types of possible modifications, structure and oxygen vacancies engineering and surface decoration were found to be crucial parameters for optimizing performances, selectivity and reaction kinetics [17–20]. Indeed, the formation of oxygen vacancies on the perovskite surface leads to better CO_2 adsorption and interaction with the catalyst, thus increasing the probability of C-O bond cleavage; abundant oxygen vacancy sites can be achieved with stoichiometry variations by synthesizing A-site-deficient perovskites, as reported in various studies [21–23]. For example, Feng et al. observed a 6-fold increase in the reaction rate for the oxidation of propane using defective structures of $LaCoO_3$ [24]; similarly, Lindenthal et al. obtained modified perovskites with Fe nanoparticles (NPs) that resulted in a CO formation-specific activity of 50 $\mu mol \cdot m^{-2} \cdot s^{-1}$, 3-fold higher than the undoped catalyst [25]. Additionally, A-site deficiency is useful to counterbalance their usually observed surface enrichment at the expense of B-site cations, the latter being redox active sites [26]. To further improve the catalytic activity of perovskites, surface decoration with active metals to form a metal–semiconductor heterostructure can be exploited [27,28]. Indeed, different studies reported that metal nanostructures or clusters deposited onto the semiconductor surface greatly enhanced the catalytic activity, due to the higher number of available active sites and the formation of Mott–Schottky junctions, enabling charge accumulation over the metallic NPs [29,30]. Moreover, the presence of different metals can result in better selectivity, as pointed out by Papargyriou et al. who observed an increase in CH_4 conversion (from 3.5% to 72%) in the dry reforming reaction in the presence of metal nanoparticles on the surface [31]. Thus, coupling perovskite semiconductors with metal nanoparticles can significantly increase the activity of the catalyst, adding different active sites that can effectively adsorb and coordinate the CO_2 molecule.

From the plethora of perovskite-based systems, lanthanum ferrite materials could be a feasible catalyst in CO_2RR, due to the high availability of raw materials, facile synthesis and non-toxicity [32,33]. To further improve the catalytic activity of $LaFeO_3$, metal deposition over the perovskite surface can be exploited; Cu and Ni are well-known transition metals for CO_2 reduction, due to their capability to interact with CO_2 and for their electronic properties [34,35]. Furthermore, these metals can act as electron trap sites, thus facilitating the charge transfer from the catalyst to the carbon dioxide molecule. Different strategies can be implemented to successfully obtain the surface deposition of metal nanoparticles; amongst them, templated incipient wetness possesses several advantages, including the possibility to use aqueous solutions and sustainable complexing agents, such as citric acid [36]. Moreover, metal dispersion and nanostructure stability have been proven to be superior to other preparation routes. Different research groups applied $LaFeO_3$-based catalysts mainly by photo-driven or electrocatalytic CO_2RR pathways [37,38]; however, a deep investigation into the thermocatalytic behavior of $LaFeO_3$-based systems is lacking. For these reasons, studying $LaFeO_3$-based systems could provide new insights into a possible active catalyst for thermal-activated CO_2RR.

In this work, $LaFeO_3$ (hereafter LFO)-based materials were synthesized and thoroughly characterized by means of several different techniques to gain information about the structural, morphological and functional properties of the systems. Moreover, Cu and Ni nanoparticles were deposited on the catalyst surface by means of the citric acid-templated wet impregnation methodology. Finally, the materials were tested as thermocatalysts for the CO_2 reduction reaction, highlighting promising catalytic activity and stability over time.

2. Results and Discussion

2.1. Structural and Morphological Characterizations

The morphology of the LFO support was characterized by N_2 physisorption and Scanning Electron Microscopy (SEM), as shown in Figure 1. The specific surface area

obtained by the Brunauer-Emmett-Teller (BET) model was 15 m^2/g, in line with other works on similar perovskite compositions and synthesis protocols. The adsorption–desorption isotherm (Figure 1a) is hybrid between a type II and type IV [39], suggesting a multilayer adsorption typical of macroporous powders as well as the presence of a massive part featured by mesoporosity, as indicated by the hysteresis loop. The pore size distribution determined by the Barrett-Joyner-Halenda (BJH) model (Figure 1b) highlighted the presence of two families of distribution both in adsorption (centered at 2.1 nm and 18 nm) and desorption (centered at 3.7 nm and 12 nm). The second is broad and predominant in both cases and features mesopores with an average width around 10–15 nm. The higher signal at a lower width in the desorption curve highlights the phenomenon called cavitation, visible also in the hysteresis curve that immediately closes between 0.4 and 0.5 of p/p^0. This behavior describes the sudden and immediate N$_2$ release by the pore with necks < 5 nm. It is visible only in the desorption curve because the N$_2$ uptake during the adsorption stage is gradual.
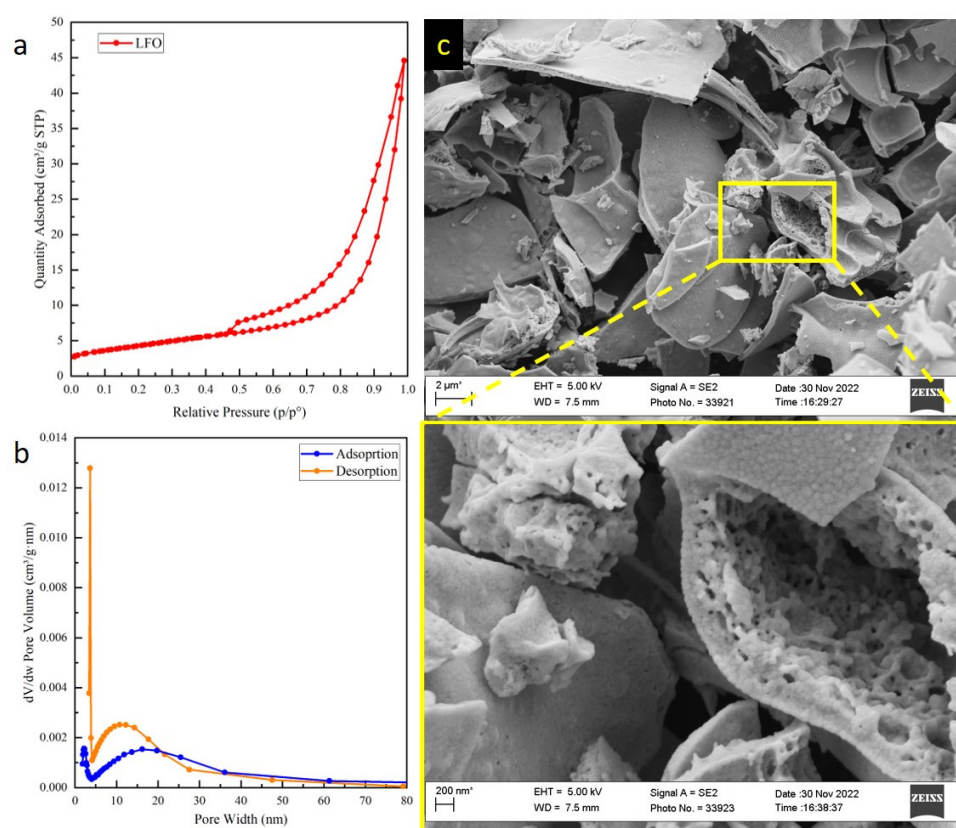

Figure 1. (**a**) The N$_2$ adsorption–desorption isotherm of the LFO support; (**b**) the corresponding pore size distribution according to the BJH model; (**c**) SEM micrographs of the calcined LFO powder at 10,000× magnification (above) and 50,000× magnification (inset below).

SEM micrographs (Figure 1c) show the appearance of big plate-like aggregates (lateral dimension in the µm range), in turn composed of grains with a size of tens of hundreds of nm. The enlargement of the detail (yellow framework) offers a more appreciable observation of meso- and macropores, evident among individual grains, in agreement with N$_2$ physisorption results. The textural features of the Ni- and Cu-loaded samples will not be further discussed because no significant changes could be appreciated by SEM, as expected, by a surface deposition technique not altering the support's morphology.

X-ray diffraction (XRD) patterns of the as-prepared (Figure 2a, left) and reduced (Figure 2a, right) catalysts showed the presence of the expected orthorhombic LaFeO$_3$ structure in all cases (COD reference 95-152-6451), without variations after the reduction treatment and preserving the perovskite structure. The deposition of rather low amounts

of Cu and/or Ni metal (4 wt%) makes the detection of the nanostructures formed during templated impregnation difficult. In fact, only a weak CuO phase could be detected at $2\theta = 35.6°$ and $38.8°$ for CuO/LFO and NiO-CuO/LFO, whereas no NiO reflections could be spotted for NiO/LFO or NiO-CuO/LFO. On the reduced catalysts, a very weak metallic reflection appeared in almost all the cases: Ni^0 at $2\theta = 44.2°$ for Ni/LFO but not for Ni-Cu/LFO; Cu^0 at $2\theta = 43.3°$ for both Cu/LFO and Ni-Cu/LFO. In general, since the reflection of copper is easier to detect, it is suggested that Cu NPs are bigger and/or less dispersed than those of Ni. Additionally, another weak reflection at $2\theta = 44.7°$ was ascribed to the formation of a Fe^0 phase in all three catalysts. This likely resulted from the reduction of segregated FeO_x species which could be present in the calcined samples for La-deficient compositions, as suggested by Schön et al. [40], not easily detectable by XRD because of the low amount and/or amorphous nature.
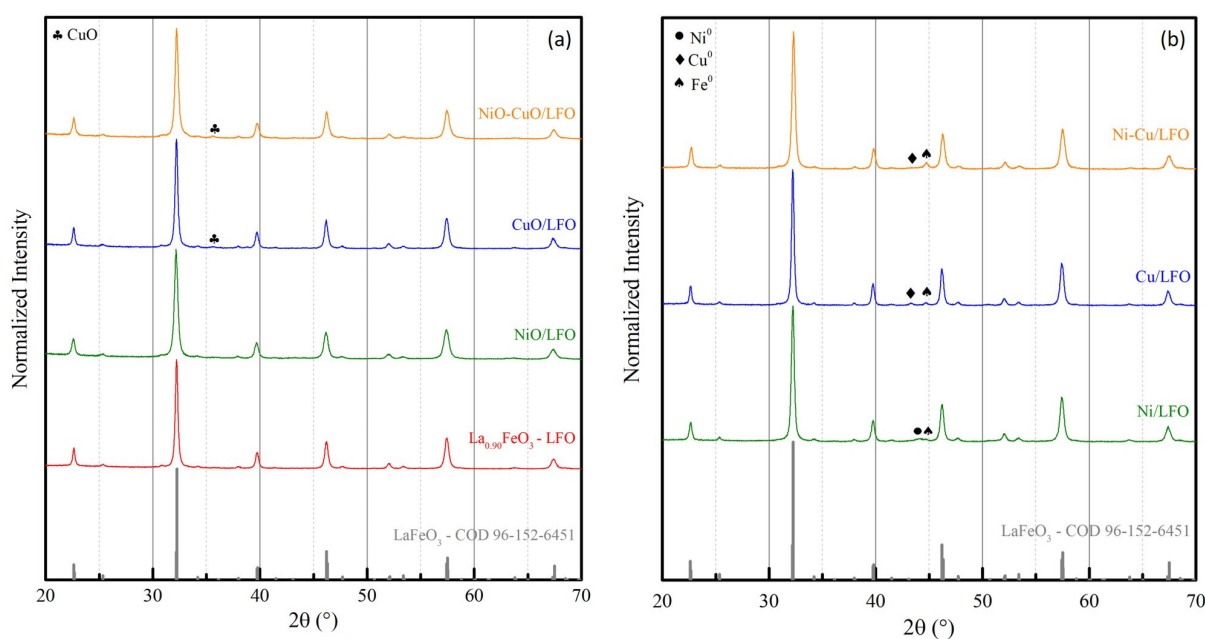

Figure 2. (**a**) XRD patterns of the as-prepared samples; (**b**) XRD patterns of the reduced samples. The reference $LaFeO_3$ structure from the COD database is also reported in gray.

The H_2-Temperature Programmed Reduction (TPR) profiles are reported in Figure 3. The bare LFO support itself displayed a multiple-step H_2 consumption in the temperature range 350–750 °C, indeed attributed to the reduction of extra-framework FeO_x species, not incorporated in the perovskite matrix; most likely, these species would be highly dispersed or amorphous Fe_2O_3 particles reducing up to Fe^0 with intermediate stoichiometries of Fe_3O_4 and FeO [40]. This result is consistent with the diffraction pattern observed for all the catalysts, confirming that A-site deficiency could lead to the formation of such spurious phases. Bulk perovskite Fe^{3+} reduction was not detected up to 900 °C, revealing a great stability of perovskite in reducing conditions. Consistently, the XRD patterns of reduced samples retained the original perovskite structure up to 600 °C; moreover, the absence of La_2O_3 diffraction patterns after reduction further confirms the stability of ferrites at high temperatures. The deposition of NiO and/or CuO particles deeply modified the reduction profiles. Ni/LFO samples displayed two broad reduction peaks centered at around 350 and 520 °C, respectively. These peaks would likely be the overlap of NiO $\rightarrow$ Ni^0 and of segregated $FeO_x \rightarrow Fe^0$ reduction events, without a clear distinction between them, in agreement with the detection of both Ni^0 and Fe^0 phases in XRD. The reduction of CuO in the Cu/LFO sample occurred in the temperature range 150–250 °C in at least two steps, with Cu^+ as a probable intermediate [41]. Furthermore, the presence of Cu greatly anticipated the reduction of extra-framework FeO_x species compared to the pristine LFO

support, with the first step already at 250 °C and the second centered at around 460 °C: this would be due to the phenomenon of H_2 spillover, i.e., H_2 facile dissociation on the surface of the pre-formed Cu^0 NPs and the subsequent transfer of H fragments to nearby FeO_x species, easing their reduction [41]. The reduction of the Fe^{3+} species of the perovskite support was also anticipated and started to be detected after 850 °C. Finally, the reduction process of Ni-Cu/LFO is more complex because of the simultaneous presence of three different transition metal species, producing a larger number of peaks/shoulders in the TPR profile. Comparing the double metal deposition profile with Cu- or Ni-deposited ferrite TPR, CuO reduction occurs in the 150–200 °C range in two steps as before, followed by another three peaks at 220, 280 and 435 °C, likely the result of both FeO_x and NiO reduction events without clear distinction between the two. Again, the phenomenon of H_2 spillover anticipates the reduction of segregated FeO_x species and, most remarkably, even the reduction of the perovskite support Fe^{3+} species, which now starts after 700 °C, i.e., at least 150 °C before all the other samples. This suggests the presence of a cooperative effect between Ni and Cu species, which are probably in stronger interaction with the perovskite support than in the cases of single Ni or Cu metals. Additionally, an easy H_2 dissociation and the subsequent migration of H fragments towards the support are possible.
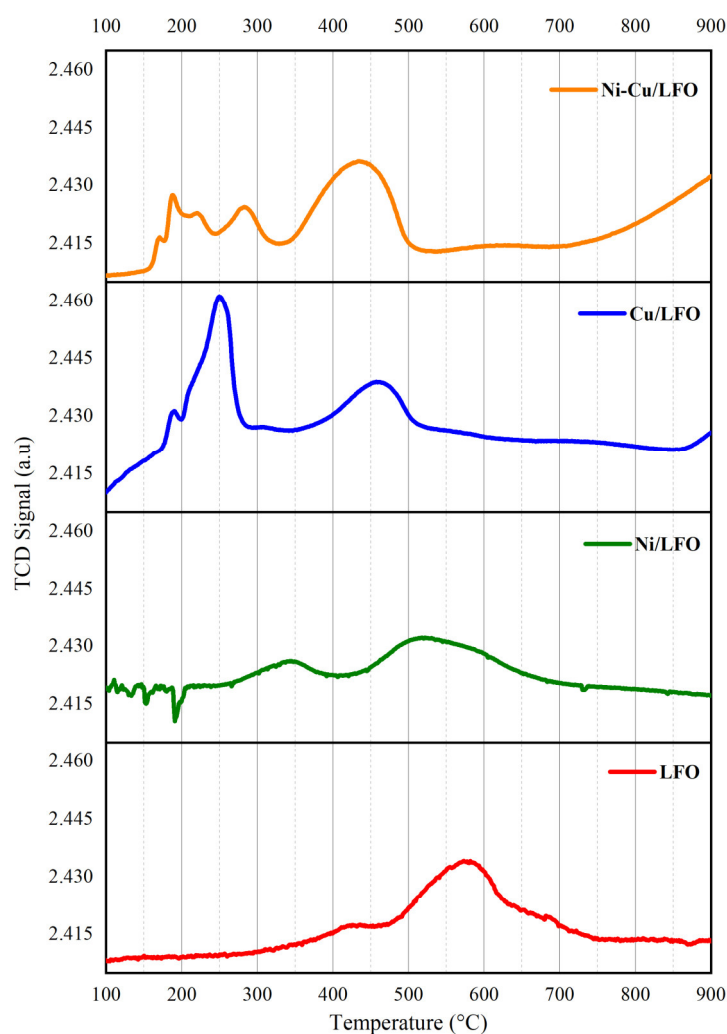

Figure 3. H_2-TPR profiles.

The CO_2-Temperature Programmed Desorption (TPD) profiles are shown in Figure 4. Two main desorption stages are discernible: the first and predominant one, centered at 70–80 °C, ascribed to CO_2 chemisorbed on weak basic sites, and the second, centered between 350 and 400 °C, ascribed to stronger basic sites. Both peaks are observed in the

bare LFO perovskite as well as on the metal-loaded samples, indicating that the adsorption sites should be located on the support surface, most likely on La^{3+} cations (possibly the low T peak) and on surface oxygen vacancies (possibly the higher T peak). However, the deposition of any kind of metal increases the intensity of both desorption stages, only to a weak extent for Cu/LFO, more pronouncedly for Ni/LFO and especially for Ni-Cu/LFO. This suggests that a higher amount of CO_2 can be chemisorbed at the metal–support interface and that the co-deposition of Ni and Cu results in a synergistic effect, in agreement with H_2-TPR.
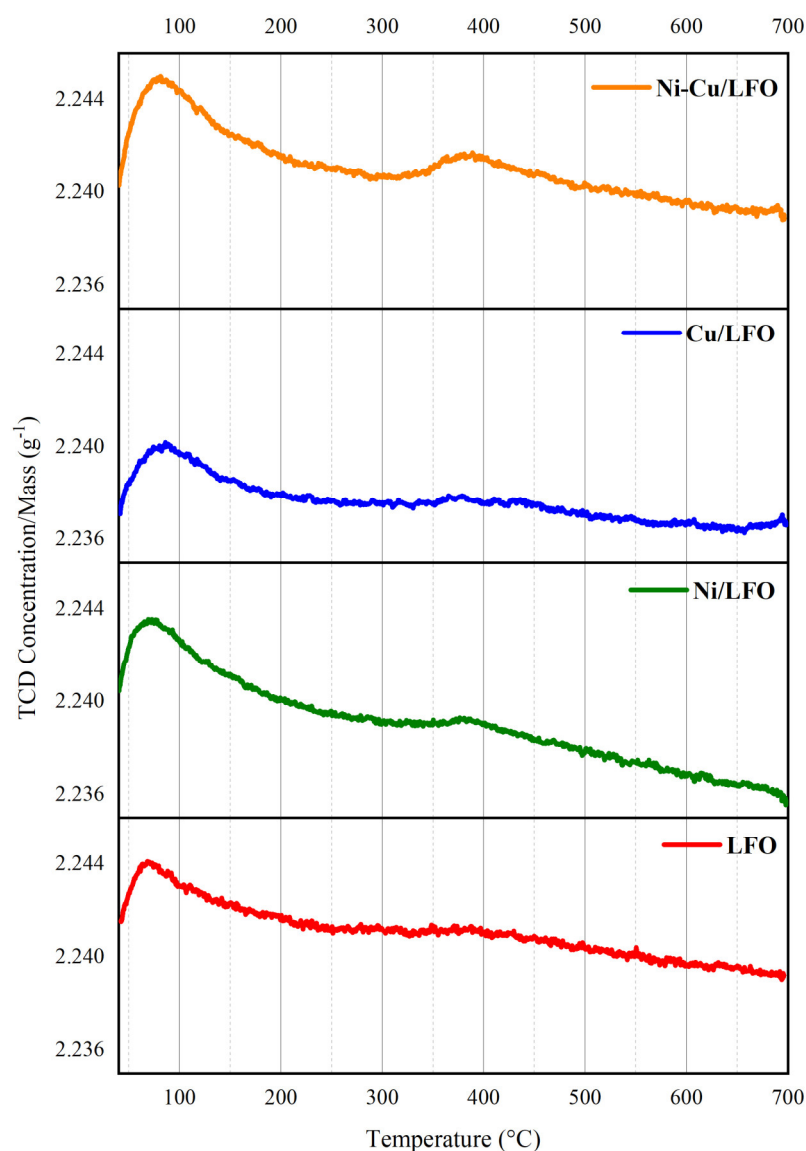

Figure 4. CO_2-TPD profiles.

2.2. Bulk and Surface Composition

The composition of the prepared catalysts was estimated by Energy Dispersive X-ray (EDX) spectroscopy concerning the bulk (ca. 1 μm of depth) and by X-ray Photoelectron Spectroscopy (XPS) for the surface (5–10 nm). The results are reported in Table 1. A surface study was carried out both on as-prepared (calcined) and reduced samples. Indeed, catalytic tests were performed after an in situ reduction of the powder catalysts, thus more representative information about the composition of the catalytic surface is provided by XPS on reduced catalysts. The amount of La in the bulk was slightly higher and that of Fe slightly lower than expected by stoichiometry, yet the La/Fe ratio was <1. On the contrary,

the surface composition in the as-prepared samples highlighted an enrichment of Fe at the expense of La (La/Fe ratio < 0.9 in all cases except Ni/LFO). Thus, on the calcined powder, there seems to exist a gradient of La and Fe concentrations in opposite directions, the former increasing going deeper towards the bulk and the latter increasing towards the surface. However, the reduction treatments inverted this tendency, enriching the surface in La at the expense of Fe and pushing the La/Fe ratio to values > 1 in all cases; although La^{3+} is a non-redox active cation, its surface enrichment might not be completely undesired since La^{3+} is a basic site capable of adsorbing CO_2, the first step for its catalytic hydrogenation.

Table 1. The bulk (EDX) and surface (XPS) composition of the prepared samples, calculated without considering the oxygen content. The nominal stoichiometric amounts are also reported between brackets.

Sample		La (at%) *	Fe (at%) *	Ni (at%) *	Cu (at%) *	La/Fe	Ni/Fe	Cu/Fe
LFO	EDX	49.5	50.5	-	-	0.98	-	-
	XPS as-prep.	44.2	55.8	-	-	0.79	-	-
	(nominal)	(44.5)	(55.5)	-	-	0.90	-	-
Ni/LFO	EDX	48.1	48.4	3.5	-	0.99	0.07	-
	XPS as-prep.	45.6	47.6	6.8	-	0.96	0.14	-
	XPS reduced	52.7	41.9	5.4	-	1.26	0.13	-
	(nominal)	(43.8)	(48.6)	(7.6)	-	(0.90)	(0.16)	-
Cu/LFO	EDX	47.8	49.3	-	2.9	0.97	-	0.06
	XPS as-prep.	35.6	46.6	-	17.8	0.76	-	0.38
	XPS reduced	41.4	36.7	-	21.9	1.13	-	0.60
	(nominal)	(44.0)	(48.9)	-	(7.1)	(0.90)	-	(0.15)
Ni-Cu/LFO	EDX	45.0	48.9	3.0	3.1	0.92	0.06	0.06
	XPS as-prep.	38.8	50.0	1.5	9.7	0.78	0.03	0.19
	XPS reduced	40.0	37.6	4.8	17.6	1.06	0.13	0.47
	(nominal)	(43.9)	(48.8)	(3.8)	(3.5)	(0.90)	(0.08)	(0.07)

* Percentage calculated without considering the oxygen content.

Regarding the single metal-deposited samples, both Ni and Cu were found in a low bulk amount compared to the expected value, while they were closer to the nominal value in the Ni-Cu-co-loaded sample. Profound differences between the two metals were observed by XPS. Cu was in a great surface excess, even more after the reduction treatment, on Cu/LFO as well as on Ni-Cu/LFO; Ni/LFO displayed a surface amount of Ni slightly defective compared to the nominal value, defectiveness which tended to increase after reduction probably because of the abnormally high segregation of La; instead, for what concerns the Ni-Cu/LFO sample, Ni was found in a very low surface amount on the calcined powder but then exceeded the theoretical amount upon reduction. In general, the tendency for both metals was to be enriched at the surface with respect to the bulk (to a much higher extent for Cu), as expected considering the procedure employed for their loading onto the LFO support, i.e., templated impregnation.

To further understand the composition as well as discover important information on nanoparticle dispersion and possible agglomeration effects, High Angle Annular Dark Field (HAADF) images and corresponding EDX maps were collected and are reported in Figure 5a–c. Ni nanoparticles in the Ni/LFO sample seem to be more dispersed and formed smaller aggregates than the counterpart Cu/LFO that clearly exhibits a minor dispersion and, in general, gives rise to bigger aggregates on the LFO support; in both cases, the maps show a good homogeneity. The most crucial result suggested by EDX maps is the higher Cu dispersion in co-impregnated Ni-Cu/LFO where it is visible that Cu does not form aggregates, compared to Cu/LFO. Not only that, but even Ni seems to receive benefits from the presence of Cu, and the agglomerates of particles are smaller than those observable in Ni/LFO. Therefore, the co-impregnation of Ni-Cu brings a better dispersion of the metals to each other on LFO, in particular for Cu. To sum up, in Figure 5d, a simple scheme of the variation in nanoparticle dispersion in all samples using the EDX maps is illustrated.
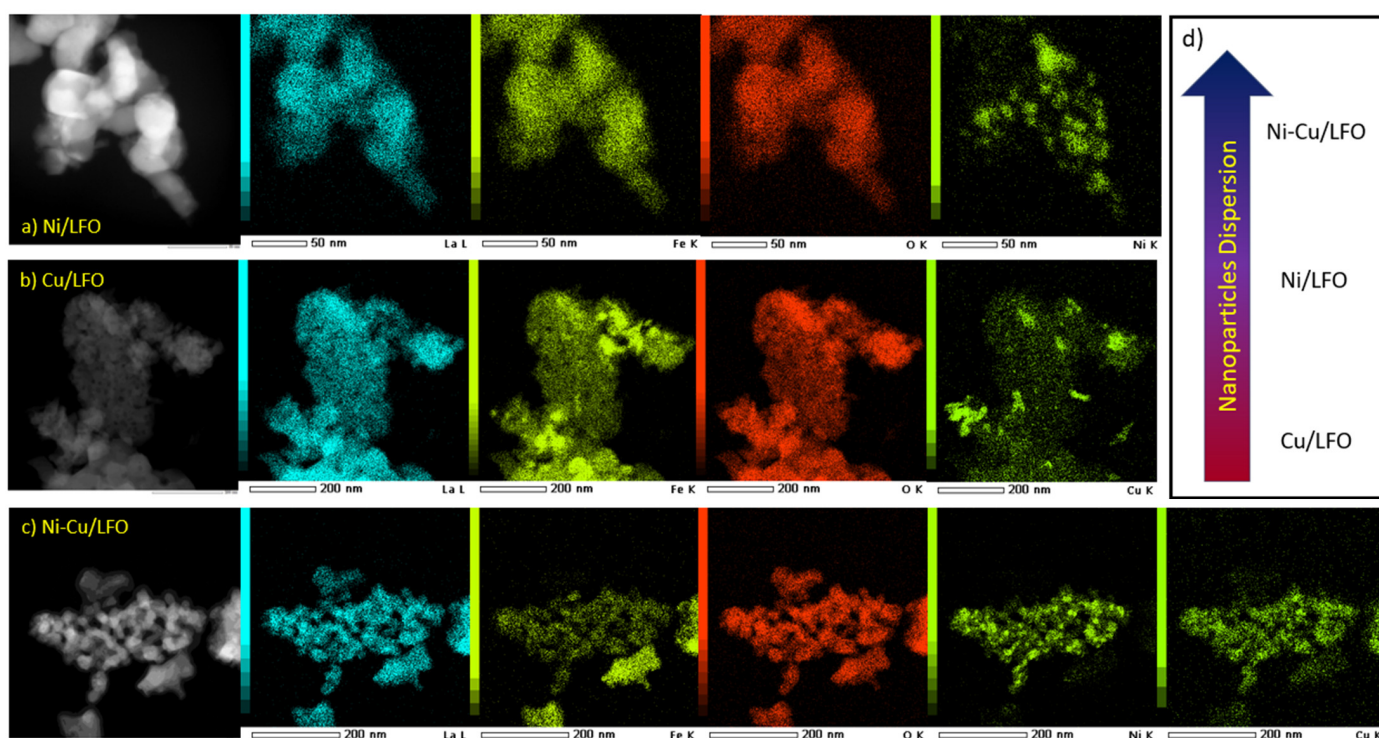
Figure 5. (**a**) Ni/LFO, (**b**) Cu/LFO, (**c**) Ni-Cu/LFO: HAADF images of the reduced samples and corresponding EDX maps of La, Fe, O, Ni and Cu; (**d**) a scheme relative to "Nanoparticles Dispersion" in all reduced samples.

2.3. Catalytic Activity

Thermocatalytic CO_2 reduction tests were performed after an in situ reduction of the catalysts under 5% H_2/Ar at 500 °C (Cu/LFO) or 600 °C (LFO, Ni/LFO and Ni-Cu/LFO), as suggested by H_2-TPR profiles (Figure 3). The inlet CO_2/H_2 ratio was 1:4. The thermochemical CO_2 conversion experiments over temperature are shown in Figure 6a–c. The bare LFO support had a discrete activity on itself, reaching almost 40% conversion at 500 °C. However, the deposition of either Ni or Cu NPs provided an increase in catalytic activity, without significant differences between the two metals, reaching about 50% CO_2 conversion at 500 °C. Notably, the co-loading of Ni and Cu was even more beneficial, allowing for an overall better CO_2 conversion below 500 °C; the onset temperature of the co-loaded catalyst was slightly lower than Cu- and Ni-deposited ferrites, thus observing higher activity towards carbon dioxide reduction. These results agree with the amount of CO_2 desorption in TPD experiments, which was enhanced after the deposition of any kind of metal compared to the LFO support but in particular for the Ni-Cu-co-loaded catalyst suggesting relating the increase in catalytic activity to the increased capability of CO_2 efficient chemisorption. Only CO was recorded as a reaction product for the pure LFO and the single metal-deposited samples, whereas CH_4 was observed as the primary product for Ni-Cu/LFO up to 370 °C. However, low-temperature condensing species, e.g., methanol, could possibly form during the reaction; as for the experimental setup, these compounds could not be quantified. This hypothesis is strengthened by the incomplete selectivity of the catalysts towards CO at higher temperature, suggesting that other products are formed but not detected. Remarkably, 100% CH_4 selectivity was obtained with Ni-Cu/LFO at T < 350 °C. After around 400 °C, CO became the major product as expected by the endothermic nature of the CO production reaction (reverse water gas shift, RWGS); regardless, the yield of CH_4 remained constantly above 10% up to 500 °C. The higher CH_4 selectivity suggests that a synergistic effect between the support material and the two metal species could be present, in agreement with H_2-TPR analysis. Indeed, looking at Figure 3, the reduction of Fe^{3+} lattice species occurs at a lower temperature in Ni-Cu/LFO because

of the higher capability of metals to dissociate H_2 into H fragments, as well as to transfer them to the active sites for CO_2 hydrogenation. Based on different literature studies, high CH_4 selectivity could be ascribed to Ni active species, while CO and CH_3OH formation could be related to Cu nanoparticles [14].
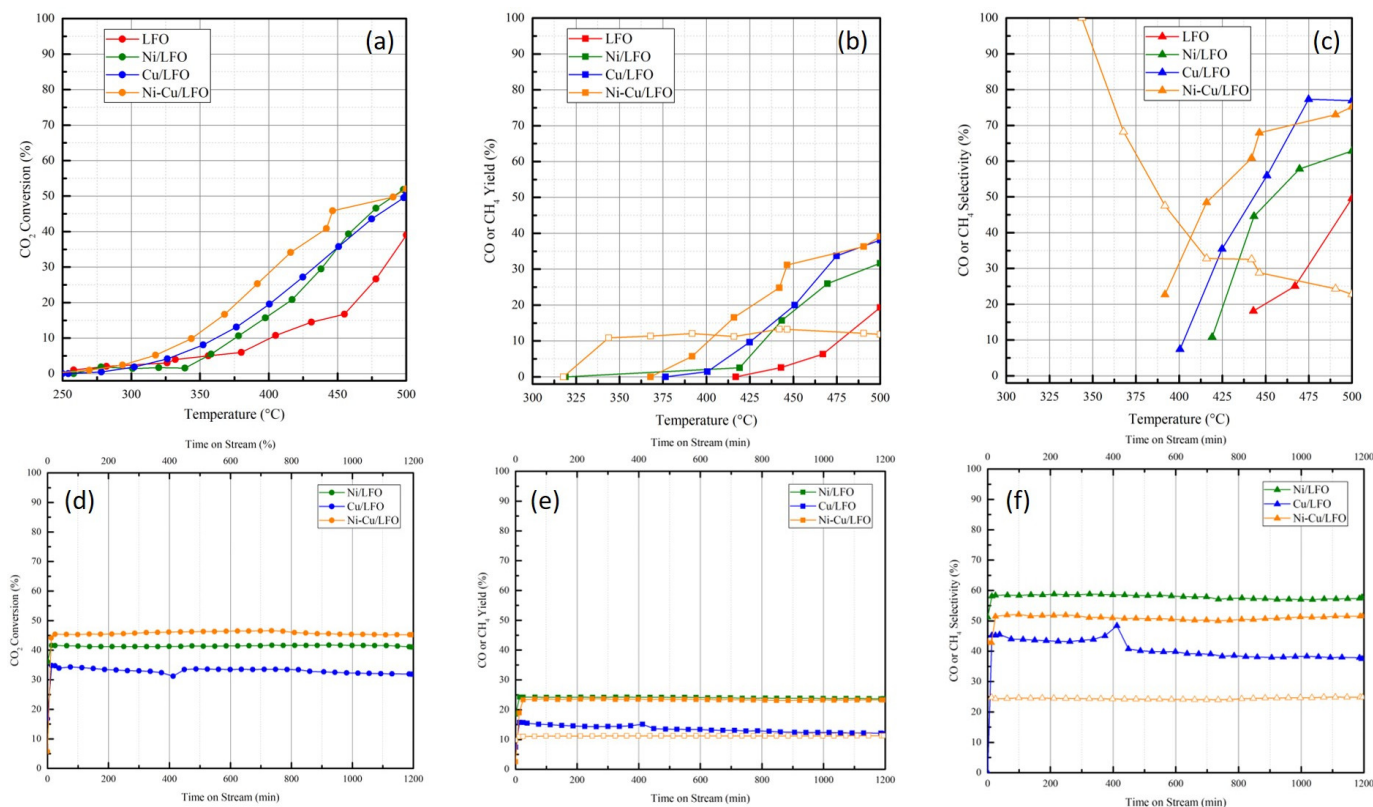

Figure 6. Thermocatalytic CO_2 conversion experiments: (**a**) CO_2 conversion vs. temperature; (**b**) CO yield (full symbols) and CH_4 yield (open symbols) vs. temperature; (**c**) CO selectivity (full symbols) and CH_4 selectivity (open symbols) vs. temperature. Stability tests over 20 h at 450 °C: (**d**) CO_2 conversion vs. time; (**e**) CO yield (full symbols) and CH_4 yield (open symbols) vs. time; (**f**) CO selectivity (full symbols) and CH_4 selectivity (open symbols) vs. time.

To address the stability of the materials in working conditions, a 20 h test was performed on all the catalysts at 450 °C (Figure 6d,e); no evident drop was observed for Ni-containing samples, while Cu/LFO showed a 5% drop in CO selectivity during the test, probably due to copper nanostructure aggregation. Indeed, the higher diffusion coefficient of Cu as well as its much higher surface concentration detected by XPS could affect the surface morphology throughout the reaction; on the other hand, the presence of Ni in Ni-Cu/LFO can result in a stabilization effect, as reported by Han et al. [42]. These outcomes are also in agreement with the EDX maps obtained by HAADF images discussed above and presented in Figure 5.

2.4. Analysis on Spent Catalysts

The spent catalysts after 20 h of reaction were characterized by XRD, as displayed in Figure 7. The orthorhombic perovskite framework was preserved in all cases, once again highlighting the stability of ferrites in reducing conditions. Ni^0 and Cu^0 phases were also detected in single-loaded catalysts, whereas no evident reflections could be spotted in the Ni-Cu-co-loaded catalyst, likely because of the lower absolute amount of each metal. Furthermore, Fe^0 reflection, which was detected on the pre-reduced samples, seemed to have disappeared or at least be much less intense on all the spent catalysts.
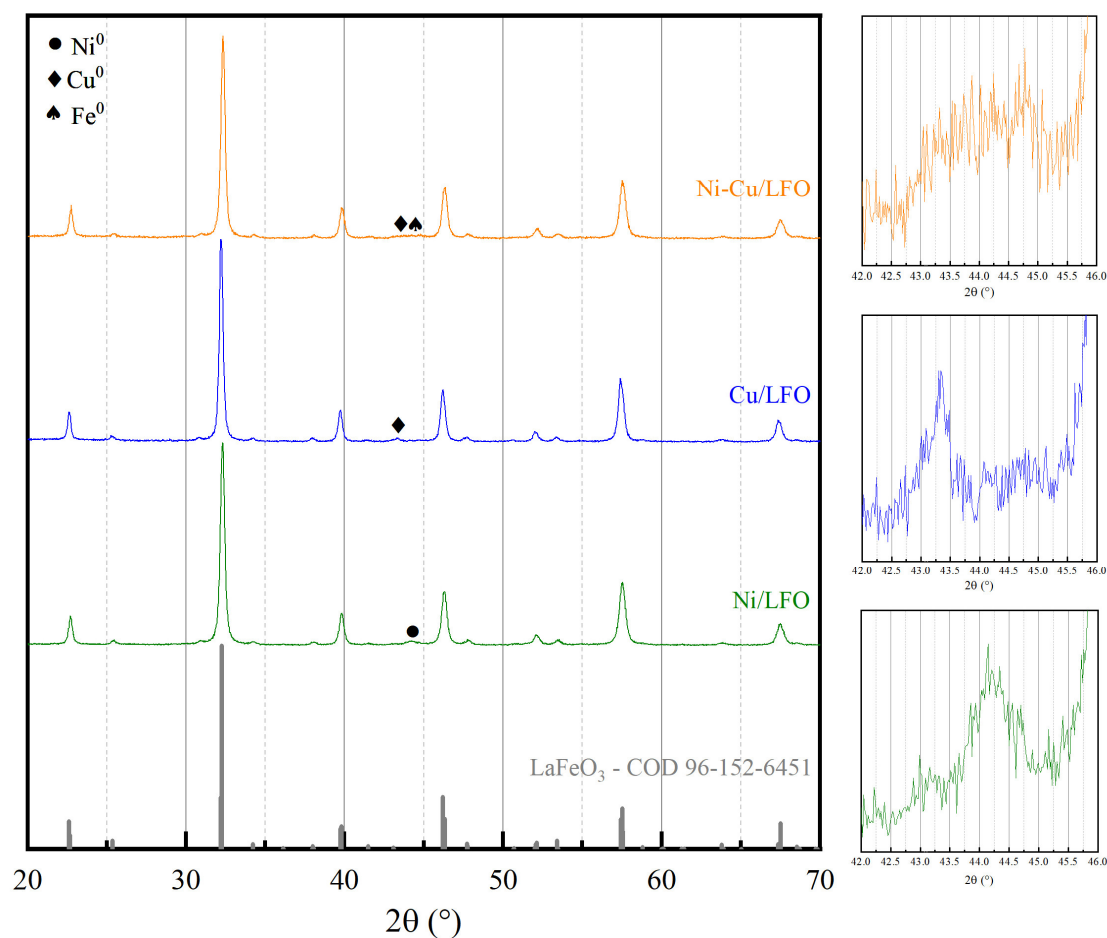
Figure 7. XRD patterns of the spent catalysts after 20 h of the reaction at 450 °C. The COD reference structure for $LaFeO_3$ perovskite is shown in gray. The enlargements of the 42°–46° (2θ) region, where the reflections of the metals can be better appreciated, are reported on the right.

An additional XPS characterization was performed on the most active Ni-Cu/LFO catalyst, comparing the pre-reduced sample (5% H_2, 600 °C) with the spent catalyst after thermochemical CO_2 reduction up to 500 °C. In Figure 8, their respective La 3d and C 1s photopeaks are displayed, whereas the Cu 2p photopeaks are shown in Figure 9. Photopeaks of the other elements are not reported because no clear differences were observed before and after the reaction; furthermore, the transition metal elements (Fe, Ni) were affected by the issue of surface reoxidation in contact with ambient air, complicating their interpretation, while the O 1s spectrum was altered by the presence of residual quartz wool after the catalytic reaction. The multiplet splitting characterizing La $3d_{5/2}$ can be useful to understand the nature of La species present on the surface and differentiate between oxide, hydroxide and carbonate, depending on the BE difference between the two contributions and on their relative intensity. The magnitude of splitting is reported to be 3.5 eV for carbonate, 3.9 eV for hydroxide and 4.6 eV for oxide; furthermore, a higher intensity of the second contribution at around 838 eV is diagnostic of carbonate, while a higher intensity of the first component around 834 eV can indicate oxide or hydroxide. In the spectra recorded for the reduced and the spent Ni-Cu/LFO catalyst, the magnitude of splitting was 3.6 eV and 3.4 eV, respectively; moreover, in both cases, the second contribution was stronger than the first one, especially for the spent catalyst. It is therefore suggested that La tends to form mainly surface carbonate species, which increase even more when exposed to a CO_2-containing atmosphere. This observation likely confirms that surface La^{3+} species of the LFO support are the predominant sites for CO_2 adsorption. The analysis of the C 1s photopeak further supports an increased amount of carbonate species after the catalytic test

compared to the reduced sample: the relative intensity of C-O and C=O contributions (at 286 and 288.5–289 eV, respectively) increases on the spent catalyst, although the C-C/C-H contribution typical of adventitious carbon (at 284.8 eV) remains the dominant component.
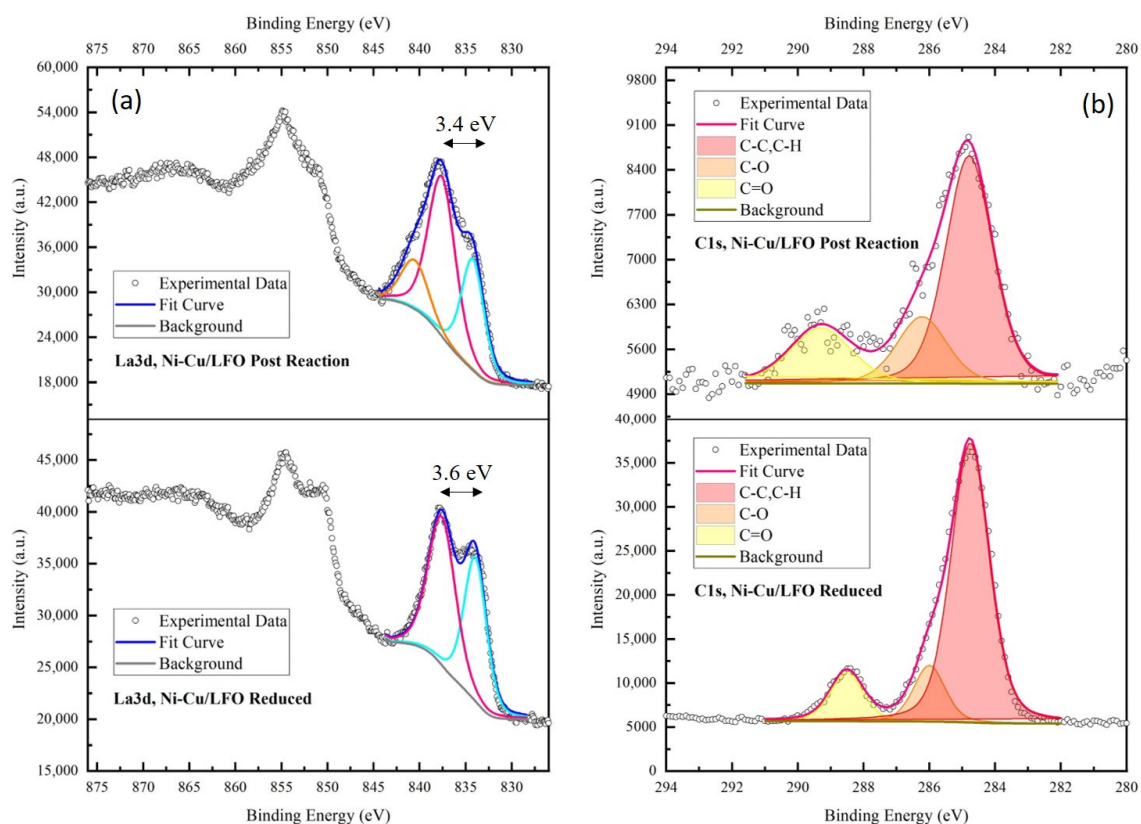

Figure 8. (**a**) The La 3d photopeak of the Ni-Cu/LFO catalyst after reduction in 5% H2/Ar at 600 °C (below) and after thermocatalytic CO_2 reduction up to 500 °C (above); (**b**) the C 1s photopeak of the Ni-Cu/LFO catalyst after reduction in 5% H_2/Ar at 600 °C (below) and after thermocatalytic CO_2 reduction up to 500 °C (above).

High-resolution Cu 2p photopeaks of the Ni-Cu/LFO sample before and after CO_2 reduction are shown in Figure 9. Before the reaction (Figure 9 below), the powder exhibits a more intense contribution at 932.7 eV due to metallic copper. However, the presence of surface Cu^{2+} was detected, and it could be due to CuO (at 933.6 eV) that covers the Cu particles because of the oxidation by atmospheric air exposure. The presence of Cu^{2+} was further confirmed by the typical Cu(II) satellite at ca. 943 eV. It is likely the presence of the amorphous copper oxide covering layer, since XRD measures do not show any reflection of CuO in the reduced powder (meaning sample Ni-Cu/LFO, Figure 2). After the reaction (Figure 9 above), instead, the contribution of Cu^{2+} slightly increases probably because of the interaction with the oxidant CO_2. However, the presence of Cu^0 can still be appreciated, although the signal is less intense than in the fresh sample (Figure 9 below). This behavior, nevertheless, does not bring any evident worsening in catalytic activity, as visible from Figure 6d–f. Therefore, the presence of Cu^{2+} cannot be avoided, but its presence seems to be influential for catalysis in the samples studied here.
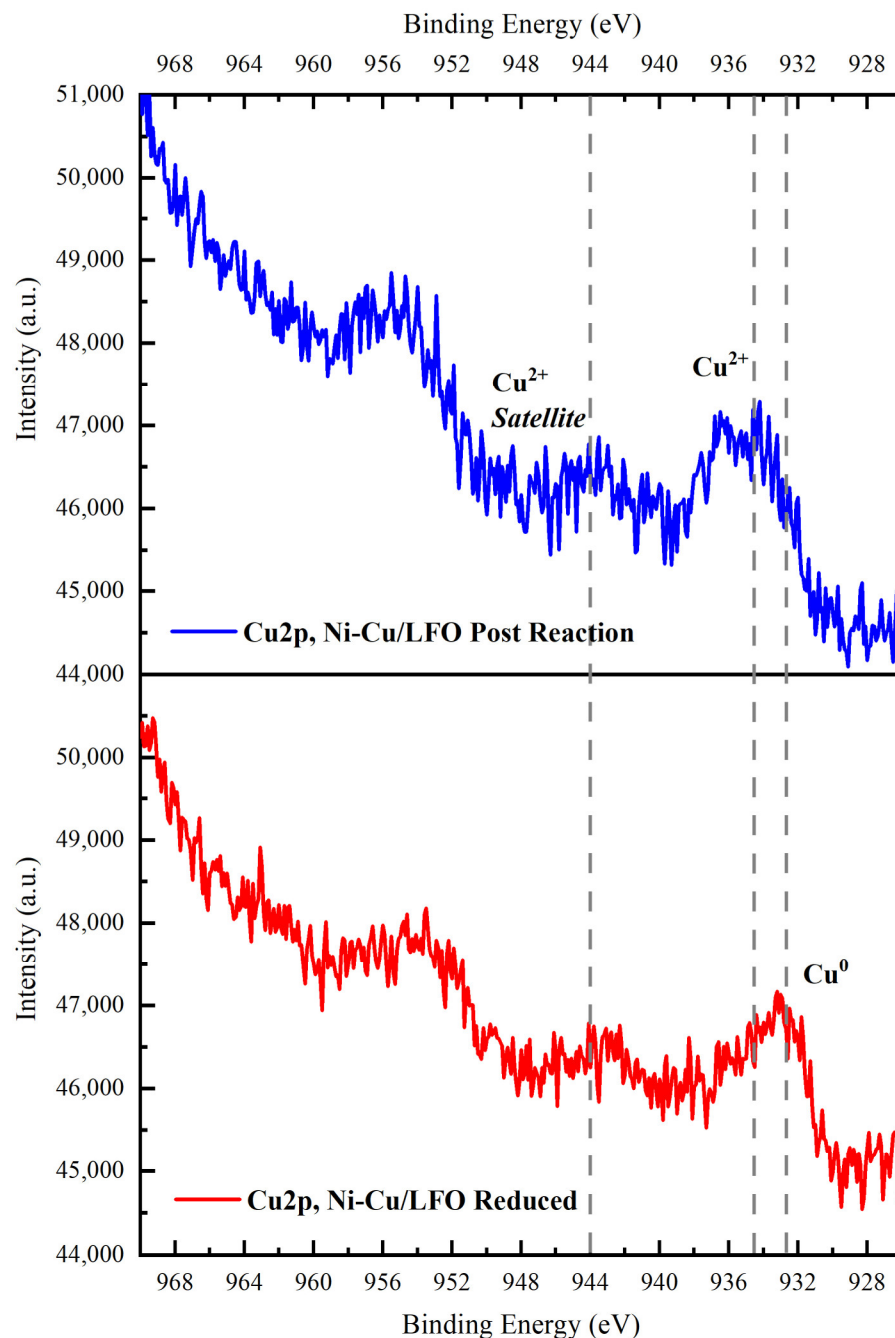
Figure 9. The Cu 2p photopeak of the Ni-Cu/LFO catalyst after reduction in 5% H_2/Ar at 600 °C (below) and after thermocatalytic CO_2 reduction up to 500 °C (above). Grey dotted lines represent the Binding Energy position (eV) of different species discussed in the text.

3. Experimental Section

3.1. Synthesis of Catalysts

The perovskite support of composition $La_{0.9}FeO_3$ (LFO) was synthesized by the sol–gel citrate route: metal precursors La_2O_3 (≥99.9% Sigma-Aldrich, Beijing, China) and $Fe(NO_3)_3 \cdot 9H_2O$ (≥99% Sigma-Aldrich, Beijing, China) were dissolved in water + HNO_3 (≥65% Sigma-Aldrich, Schnelldorf, Germany), with a molar ratio of $La^{3+}/(NO_3)$ = 1:3 (equivalent to lanthanum nitrate salt), by heating at 150 °C; after cooling down to approximately 50 °C, citric acid monohydrate (CA, ≥99.0% Sigma-Aldrich, Vienna, Austria) was added according to a molar ratio CA/(La + Fe) of 1.5. The solvent was then evaporated at 120 °C overnight, thus obtaining a gel; after its complete dehydration, the temperature

was raised to 300 °C to trigger gel decomposition by autoignition. The resulting solid was grinded to a powder and ultimately calcined at 600 °C (heating ramp: 5 °C/min) for 6 h under static air. The specific surface area of the calcined powder was 15 m^2/g, as determined by the BET method from N_2 physisorption analysis.

Ni and Cu deposition was performed by citric acid-templated wet impregnation: the required amount of metal precursors, i.e., $Ni(NO_3)_2 \cdot 6H_2O$ ($\geq$97.0% Sigma-Aldrich, Schnelldorf, Germany) and/or $Cu(NO_3)_2 \cdot 3H_2O$ ($\geq$99.0% Sigma-Aldrich, Schnelldorf, Germany) was dissolved in water, and 2 g of the perovskite support was suspended in the prepared solution by magnetic stirring. Citric acid was then added, following a CA/metal (Ni, Cu or Ni + Cu) molar ratio of 1.0. The next steps proceeded analogously to $La_{0.9}FeO_3$ synthesis (gel formation and decomposition). A final calcination at 400 °C for 4 h (heating ramp: 5 °C/min) was carried out to obtain NiO and/or CuO particles supported over LFO. Three different samples were prepared: $Ni/La_{0.9}FeO_3$ (4 wt% Ni), $Cu/La_{0.9}FeO_3$ (4 wt% Cu) and $Ni-Cu/La_{0.9}FeO_3$ (2 wt% Ni-2 wt% Cu). The samples will be named Ni/LFO, Cu/LFO and Ni-Cu/LFO, respectively.

A fraction of each catalyst (ca. 100 mg), loaded in a U-shaped quartz reactor above a plug of quartz wool, was reduced under 5 vol% H_2/Ar for 2 h, at a temperature determined by H_2-TPR experiments (500 °C for Cu/LFO, 600 °C for Ni/LFO and Ni-Cu/LFO), to obtain metallic NPs of Ni, Cu and Fe as well.

3.2. Characterizations

Powder X-ray diffraction (XRD) patterns were acquired in the 2θ range of 20–80° with a Bruker D8 Advanced diffractometer in Bragg–Brentano geometry, employing a Cu Kα source (λ = 1.5406 Å), powered at 40 kV and 40 mA, with steps of 0.02° and dwell time 0.35 s/step. Both as-prepared and reduced samples were analyzed.

N_2 physisorption analysis was performed on a ASAP2020 PLUS instrument (Micromeritics, Norcross, GA, USA). The LFO support (600 mg) was first outgassed under vacuum (P < 10 μmHg) at 300 °C for 3 h; then, N_2 physisorption was measured at −196 °C in the relative pressure range of 0.01–0.995. The specific surface area was determined by the BET method and the pore size distribution by the BJH method.

H_2 temperature-programmed reduction (TPR) was carried out to investigate the materials' reducibility, on a Autochem II 2920 instrument (Micromeritics, Norcross, GA, USA). A total of 50 mg of the sample was loaded on a U-shaped quartz reactor, above a layer of quartz wool, and heated from RT to 950 °C (ramp 10 °C/min) under a 50 cm^3/min flow of 5% H_2/Ar. H_2 consumption was monitored with a TCD detector after H_2O absorption by a cold trap.

The same apparatus and setup were employed for CO_2 temperature-programmed desorption (TPD) experiments. A total of 100 mg of samples was first outgassed under He flow (50 cm^3/min) at 300 °C for 1 h and cooled down to 40 °C in the same environment. Subsequently, 20 cm^3/min of CO_2 was allowed to adsorb on the sample surface for 30 min. Finally, after 10 min of purging with He (20 cm^3/min) to remove weakly physiosorbed CO_2, the TPD profiles were recorded under 50 cm^3/min of He while heating from 40 to 700 °C at 5 °C/min.

Scanning electron microscopy (SEM) images were acquired with a SUPRA 40 V P microscope (Zeiss, Oberkochen, Germany), at an electron acceleration voltage of 5 kV. Energy-dispersive X-ray analysis (EDX) was coupled to SEM for elemental quantification, at a 20 kV electron acceleration voltage; the X-ray peaks considered for quantification were O Kα, Fe Kα, La Lα, Ni Kα and Cu Kα. Only the as-prepared samples were analyzed by this method, since no significant changes in the perovskite morphology and element quantification were to be expected after a relatively short reduction treatment.

High-Angle Annular Dark Field (HAADF) images and the corresponding EDX maps were collected by a JEM-F200 (JEOL, Tokyo, Japan) in Scanning Transmission Electron Microscopy (STEM) mode using an accelerating voltage of 200 kV; the X-ray peaks considered were La L, Fe K, O K, Ni K and Cu K. The preparation of the samples involved the

dispersion of the powders in ethanol by sonication and the deposition of a few drops of the dispersion on a carbon-coated Au grid.

X-ray photoelectron spectroscopy (XPS) was performed on the as-prepared and reduced catalysts with a ESCALAB QXi spectrometer (Thermo Fischer, Waltham, MA, USA), employing a monochromatized Al Kα source (hν = 1486.68 eV) and a charge compensation gun. The spectrometer was calibrated by assuming the binding energy (BE) of the Au 4f$_{7/2}$ line to be 84.0 eV with respect to the Fermi level. To take into account any residual charging, the BE scale was corrected by setting the adventitious carbon C 1s photopeak at 284.8 eV. Survey spectra were acquired at pass energy 100 eV, 0.5 eV/step and dwell time 50 ms/step. Detailed spectra were recorded at 20 eV pass energy, 0.1 eV/step and dwell time 25 ms/step. Elemental quantification was carried out by the integration of La 3d$_{5/2}$, Fe 2p, O 1s, Ni 3p and Cu 2p photopeaks, after Shirley-type background subtraction.

3.3. Catalytic Tests

The prepared catalysts were tested for thermocatalytic CO_2 reduction. A fixed bed quartz reactor (ID 6 mm) was employed, loading 50 mg of the sample between two layers of quartz wool, and a K-type thermocouple was placed in contact with the catalyst bed to monitor its temperature. The catalysts were firstly reduced in situ under 5 vol% H_2/Ar at 500 °C (for Cu/LFO) or 600 °C (for LFO, Ni/LFO and Ni-Cu/LFO), stationing 2 h at the target T. After this step, the catalysts were cooled down to 200 °C, and the reaction mixture was introduced, composed of 2 vol% CO_2, 8 vol% H_2 and Ar balance, with total flow rate 100 cm^3/min (weighted hourly space velocity, WHSV = 120 L/h/g). For thermochemical CO_2 conversion experiments, the temperature was raised from 200 to 500 °C at 2 °C/min, whereas for stability tests, the temperature was increased to 450 °C at 10 °C/min and kept at this value for 20 h. The outlet gas mixture was analyzed by an online GC 7890A (Agilent, Santa Clara, CA, USA), equipped with a TCD detector and two packed columns, Porapak Q (80/100 mesh, 1.8 m) for CH_4 and CO_2 detection and MolSieve 13X (60/80 mesh, 1.8 m) for CO detection, using He as a carrier gas. Before reaching the GC, a chiller was used to trap the generated H_2O and other condensable molecules, such as CH_3OH.

The conversion of CO_2 (X_{CO_2}), the selectivity (S_i) and the yield (Y_i) of the i-th product were calculated according to Equation (1), Equation (2) and Equation (3), respectively.

$$X_{CO_2}(\%) = 100 \times (F_{CO2,0} - F_{CO2,t})/F_{CO2,0} \tag{1}$$

$$S_i(\%) = 100 \times F_{i,t}/(F_{CO2,0} - F_{CO2,t}) \tag{2}$$

$$Y_i(\%) = 100 \times F_{i,t}/F_{CO2,0} \tag{3}$$

$F_{CO2,0}$ denotes the inlet flow rate of CO_2 (2 cm^3/min), $F_{CO2,t}$ the outlet flow rate of CO_2 at a given time or temperature and $F_{i,t}$ the outlet flow rate of the i-th product (CO or CH_4) at a given time or temperature, as quantified by GC.

4. Conclusions

Concerning emissions and concentrations of CO_2 need to be tackled to avoid further environmental damage and disasters. A possible solution is to convert CO_2 by transforming it into fuels, such as CH_4 and CO, via CO_2RR through proper catalyst design.

In this work, the La$_{0.9}$FeO$_3$ perovskite support was prepared via the sol–gel citrate route and then loaded by citric acid-templated wet impregnation with Ni, Cu and Ni-Cu to prepare three different catalysts. XRD analysis highlights that the orthorhombic structure of LaFeO$_3$ was preserved also after the reducing treatment suggesting the robustness of the catalysts in the reaction environment, also confirmed by H_2-TPR analysis. Subsequently, the materials were tested for thermocatalytic CO_2RR: Ni and Cu reached 50% of CO_2 conversion at 500 °C, while Ni-Cu-co-loaded LFO achieved the same conversion at a lower temperature. These results agree with the amount of CO_2 desorption in TPD experiments that highlight that Ni-Cu is capable to adsorb more CO_2 than other catalysts as well as the bare support. XPS analysis on the Ni-Cu/LFO spent catalyst detected that surface La^{3+}

species of the LFO support are the predominant sites for CO_2 adsorption. In addition, Ni-Cu/LFO exhibits both higher activity towards H_2 dissociation in fragmented H, which participates in CO_2 hydrogenation, and low NP agglomeration, as also observed from HAADF images and the corresponding EDX maps. These results allow us to correlate the higher activity towards CO_2RR of this catalyst with the capability of adsorbing the CO_2 of co-loaded metals and the support suggesting a possible synergic interaction. Even outstanding 100% CH_4 selectivity was gained with Ni-Cu/LFO below 350 °C, corroborating the hypothesis of a synergistic effect between the support material and the impregnated Ni-Cu. Finally, the three catalysts, as well as the bare LFO support, exhibit a notably durability after 20 h on the reaction stream at 450 °C; no evident drop was observed for Ni-containing samples, while Cu/LFO showed a 5% drop in CO selectivity during the test, probably due to the sintering of copper nanostructures. However, the presence of Ni in Ni-Cu/LFO can result in a stabilization effect.

Author Contributions: Conceptualization, A.M. and A.O.; methodology, A.G.; validation, A.O., J.C. and L.R.; formal analysis, A.M. and A.O.; investigation, A.M., A.O. and J.C.; resources, A.G.; visualization: L.R. and J.C.; writing—original draft preparation, A.O., J.C. and L.R.; writing—review and editing, A.M. and A.G.; supervision, A.G.; project administration, A.G.; funding acquisition, A.G. All authors have read and agreed to the published version of the manuscript.

Data Availability Statement: All data are available upon request by contacting the corresponding author: jonathan.cavazzani@phd.unipd.it.

Conflicts of Interest: The authors declare no conflicts of interest. The funders had no role in the design of the study; in the collection, analyses or interpretation of data; in the writing of the manuscript; or in the decision to publish the results.

References

1. Shukla, P.R.; Skea, J.; Buendia, E.C.; Masson-Delmotte, V.; Pörtner, H.-O.; Roberts, D.C.; Zhai, P.; Slade, R.; Connors, S.; van Diemen, R.; et al. *IPCC, 2019 Climate Change and Land: An IPCC Special Report on Climate Change, Desertification, Land Degradation, Sustainable Land Management, Food Security, and Greenhouse Gas Fluxes in Terrestrial Ecosystems*; Cambridge University Press: Cambridge, UK, 2019.

2. Hasegawa, T.; Sakurai, G.; Fujimori, S.; Takahashi, K.; Hijioka, Y.; Masui, T. Extreme Climate Events Increase Risk of Global Food Insecurity and Adaptation Needs. *Nature Food* **2021**, *2*, 587–595. [CrossRef] [PubMed]

3. Yoro, K.O.; Daramola, M.O. CO_2 Emission Sources, Greenhouse Gases, and the Global Warming Effect. In *Advances in Carbon Capture Methods, Technologies and Applications*; Elsevier: Amsterdam, The Netherlands, 2020; pp. 3–28. [CrossRef]

4. Valluri, S.; Claremboux, V.; Kawatra, S. Opportunities and Challenges in CO_2 Utilization. *J. Environ. Sci.* **2022**, *113*, 322–344. [CrossRef] [PubMed]

5. Takht Ravanchi, M.; Sahebdelfar, S. Catalytic Conversions of CO_2 to Help Mitigate Climate Change: Recent Process Developments. *Process Saf. Environ. Prot.* **2021**, *145*, 172–194. [CrossRef]

6. Li, K.; Peng, B.; Peng, T. Recent Advances in Heterogeneous Photocatalytic CO_2 Conversion to Solar Fuels. *ACS Catal.* **2016**, *6*, 7485–7527. [CrossRef]

7. Zheng, Y.; Zhang, W.; Li, Y.; Chen, J.; Yu, B.; Wang, J.; Zhang, L.; Zhang, J. Energy Related CO_2 Conversion and Utilization: Advanced Materials/Nanomaterials, Reaction Mechanisms and Technologies. *Nano Energy* **2017**, *40*, 512–539. [CrossRef]

8. Hightower, F.W.; White, A.H. Synthesis of Methane from Water Gas. *Ind. Eng. Chem.* **1928**, *20*, 10–15. [CrossRef]

9. Meng, X.; Wang, T.; Liu, L.; Ouyang, S.; Li, P.; Hu, H.; Kako, T.; Iwai, H.; Tanaka, A.; Ye, J. Photothermal Conversion of CO_2 into CH_4 with H_2 over Group VIII Nanocatalysts: An Alternative Approach for Solar Fuel Production. *Angew. Chem. Int. Ed.* **2014**, *53*, 11478–11482. [CrossRef] [PubMed]

10. Song, C. Global Challenges and Strategies for Control, Conversion and Utilization of CO_2 for Sustainable Development Involving Energy, Catalysis, Adsorption and Chemical Processing. *Catal. Today* **2006**, *115*, 2–32. [CrossRef]

11. Salehizadeh, H.; Yan, N.; Farnood, R. Recent Advances in Microbial CO_2 Fixation and Conversion to Value-Added Products. *Chem. Eng. J.* **2020**, *390*, 124584. [CrossRef]

12. Tabish, A.; Varghese, A.M.; Wahab, M.A.; Karanikolos, G.N. Perovskites in the Energy Grid and CO_2 Conversion: Current Context and Future Directions. *Catalysts* **2020**, *10*, 95. [CrossRef]

13. Irvine, J.; Rupp, J.L.M.; Liu, G.; Xu, X.; Haile, S.; Qian, X.; Snyder, A.; Freer, R.; Ekren, D.; Skinner, S.; et al. Roadmap on Inorganic Perovskites for Energy Applications. *J. Phys. Energy* **2021**, *3*, 031502. [CrossRef]

14. Rizzato, L.; Cavazzani, J.; Osti, A.; Scavini, M.; Glisenti, A. Cu-Doped $SrTiO_3$ Nanostructured Catalysts for CO_2 Conversion into Solar Fuels Using Localised Surface Plasmon Resonance. *Catalysts* **2023**, *13*, 1377. [CrossRef]

15. Bhattacharya, K.; Ravichandran, G. Ferroelectric Perovskites for Electromechanical Actuation. *Acta Mater.* **2003**, *51*, 5941–5960. [CrossRef]

16. *Properties and Applications of Perovskite-Type Oxides*; CRC Press: Boca Raton, FL, USA, 1993.

17. Wang, Z.; Huang, H.; Li, G.; Yan, X.; Yu, Z.; Wang, K.; Wu, Y. Advances in Engineering Perovskite Oxides for Photochemical and Photoelectrochemical Water Splitting. *Appl. Phys. Rev.* **2021**, *8*, 021320. [CrossRef]

18. Sun, Y.; Yang, J.; Li, S.; Wang, D. Defect Engineering in Perovskite Oxide Thin Films. *Chem. Commun.* **2021**, *57*, 8402–8420. [CrossRef] [PubMed]

19. Ji, Q.; Bi, L.; Zhang, J.; Cao, H.; Zhao, X.S. The Role of Oxygen Vacancies of ABO_3 Perovskite Oxides in the Oxygen Reduction Reaction. *Energy Environ. Sci.* **2020**, *13*, 1408–1428. [CrossRef]

20. Ruh, T.; Berkovec, D.; Schrenk, F.; Rameshan, C. Exsolution on Perovskite Oxides: Morphology and Anchorage of Nanoparticles. *Chem. Commun.* **2023**, *59*, 3948–3956. [CrossRef] [PubMed]

21. Zhang, J.; Xie, K.; Wei, H.; Qin, Q.; Qi, W.; Yang, L.; Ruan, C.; Wu, Y. In Situ Formation of Oxygen Vacancy in Perovskite $Sr_{0.95}Ti_{0.8}Nb_{0.1}M_{0.1}O_3$ (M = Mn, Cr) toward Efficient Carbon Dioxide Electrolysis. *Sci. Rep.* **2014**, *4*, 7082. [CrossRef] [PubMed]

22. Gao, Y.; Zhang, M.; Jin, Y.; Zhou, M.; Mao, Y.; Sun, J.; Wang, W.; Song, Z. Low-Coordination Transition Metal Sites on Oxygen Vacancy Enriched Strontium Titanate-Based Perovskites Enable Highly Selective Photocatalytic CO_2 Reduction to CH_4. *Appl. Catal. B* **2024**, *341*, 123348. [CrossRef]

23. Kozokaro, V.F.; Addo, P.K.; Ansari, H.M.; Birss, V.I.; Toroker, M.C. Optimal Oxygen Vacancy Concentration for CO_2 Reduction in LSFCR Perovskite: A Combined Density Functional Theory and Thermogravimetric Analysis Measurement Study. *J. Phys. Chem. C* **2020**, *124*, 27453–27466. [CrossRef]

24. Feng, C.; Gao, Q.; Xiong, G.; Chen, Y.; Pan, Y.; Fei, Z.; Li, Y.; Lu, Y.; Liu, C.; Liu, Y. Defect Engineering Technique for the Fabrication of $LaCoO_3$ Perovskite Catalyst via Urea Treatment for Total Oxidation of Propane. *Appl. Catal. B* **2022**, *304*, 121005. [CrossRef]

25. Lindenthal, L.; Popovic, J.; Rameshan, R.; Huber, J.; Schrenk, F.; Ruh, T.; Nenning, A.; Löffler, S.; Opitz, A.K.; Rameshan, C. Novel Perovskite Catalysts for CO_2 Utilization—Exsolution Enhanced Reverse Water-Gas Shift Activity. *Appl. Catal. B* **2021**, *292*, 120183. [CrossRef]

26. Liu, J.; Kim, J.K.; Wang, Y.; Kim, H.; Belotti, A.; Koo, B.; Wang, Z.; Jung, W.C.; Ciucci, F. Understanding and Mitigating A-Site Surface Enrichment in Ba-Containing Perovskites: A Combined Computational and Experimental Study of $BaFeO_3$. *Energy Environ. Sci.* **2022**, *15*, 4069–4082. [CrossRef]

27. Shyamal, S.; Dutta, S.K.; Das, T.; Sen, S.; Chakraborty, S.; Pradhan, N. Facets and Defects in Perovskite Nanocrystals for Photocatalytic CO2Reduction. *J. Phys. Chem. Lett.* **2020**, *11*, 3608–3614. [CrossRef] [PubMed]

28. Hu, C.; Hong, J.; Huang, J.; Chen, W.; Segre, C.U.; Suenaga, K.; Zhao, W.; Huang, F.; Wang, J. Surface Decoration Accelerates the Hydrogen Evolution Kinetics of a Perovskite Oxide in Alkaline Solution. *Energy Environ. Sci.* **2020**, *13*, 4249–4257. [CrossRef]

29. Zhang, J.; Wang, Y.; Tian, J.; Yan, B. Cu/$LaFeO_3$ as an Efficient and Stable Catalyst for CO_2 Reduction: Exploring Synergistic Effect between Cu and $LaFeO_3$. *AIChE J.* **2022**, *68*, e17640. [CrossRef]

30. Schrenk, F.; Lindenthal, L.; Pacholik, G.; Navratil, T.; Berger, T.M.; Drexler, H.; Rameshan, R.; Ruh, T.; Föttinger, K.; Rameshan, C. Perovskite-Type Oxide Catalysts in CO_2 Utilization: A Principal Study of Novel Cu-Doped Perovskites for Methanol Synthesis. *Compounds* **2022**, *2*, 378–387. [CrossRef]

31. Papargyriou, D.; Miller, D.N.; Irvine, J.T.S. Exsolution of Fe–Ni Alloy Nanoparticles from (La,Sr)(Cr,Fe,Ni)O_3 Perovskites as Potential Oxygen Transport Membrane Catalysts for Methane Reforming. *J. Mater. Chem. A Mater.* **2019**, *7*, 15812–15822. [CrossRef]

32. Ivanov, D.V.; Pinaeva, L.G.; Isupova, L.A.; Nadeev, A.N.; Prosvirin, I.P.; Dovlitova, L.S. Insights into the Reactivity of $La_{1-X}Sr_xMnO_3$ (x = 0 ÷ 0.7) in High Temperature N_2O Decomposition. *Catal. Lett.* **2011**, *141*, 322–331. [CrossRef]

33. Huang, X.; Zhao, G.; Wang, G.; Irvine, J.T.S. Synthesis and Applications of Nanoporous Perovskite Metal Oxides. *Chem. Sci.* **2018**, *9*, 3623–3637. [CrossRef]

34. Hou, Y.; Liang, Y.L.; Shi, P.C.; Huang, Y.B.; Cao, R. Atomically Dispersed Ni Species on N-Doped Carbon Nanotubes for Electroreduction of CO_2 with Nearly 100% CO Selectivity. *Appl. Catal. B* **2020**, *271*, 118929. [CrossRef]

35. Li, H.; Wei, P.; Gao, D.; Wang, G. In Situ Raman Spectroscopy Studies for Electrochemical CO_2 Reduction over Cu Catalysts. *Curr. Opin. Green Sustain. Chem.* **2022**, *34*, 100589. [CrossRef]

36. Carollo, G.; Garbujo, A.; Bedon, A.; Ferri, D.; Natile, M.M.; Glisenti, A. Cu/CGO Cermet Based Electrodes for Symmetric and Reversible Solid Oxide Fuel Cells. *Int. J. Hydrogen Energy* **2020**, *45*, 13652–13658. [CrossRef]

37. Hu, S.; Zhang, L.; Liu, H.; Cao, Z.; Yu, W.; Zhu, X.; Yang, W. Alkaline-Earth Elements (Ca, Sr and Ba) Doped $LaFeO_{3-\delta}$ Cathodes for CO_2 Electroreduction. *J. Power Sources* **2019**, *443*, 227268. [CrossRef]

38. Ibarra-Rodriguez, L.I.; Garay-Rodríguez, L.F.; Torres-Martínez, L.M. Photocatalytic Reduction of CO_2 over $LaMO_3$ (M: Fe, Co, Mn) /CuxO Films. *Mater. Sci. Semicond. Process.* **2022**, *139*, 106328. [CrossRef]

39. Thommes, M.; Kaneko, K.; Neimark, A.V.; Olivier, J.P.; Rodriguez-Reinoso, F.; Rouquerol, J.; Sing, K.S. Physisorption of gases, with special reference to the evaluation of surface area and pore size distribution (IUPAC Technical Report). *Pure Appl. Chem.* **2015**, *87*, 1051–1069. [CrossRef]

40. Schön, A.; Dujardin, C.; Dacquin, J.P.; Granger, P. Enhancing catalytic activity of perovskite-based catalysts in three-way catalysis by surface composition optimisation. *Catal. Today* **2015**, *258*, 543–548. [CrossRef]

41. Esmaeilnejad-Ahranjani, P.; Khodadadi, A.A.; Mortazavi, Y. Self-regenerative function of Cu in $LaMnCu_{0.1}O_3$ catalyst: Towards noble metal-free intelligent perovskites for automotive exhaust gas treatment. *Appl. Catal. A Gen.* **2020**, *602*, 117702. [CrossRef]

42. Han, K.; Wang, S.; Hu, N.; Shi, W.; Wang, F. Alloying Ni–Cu nanoparticles encapsulated in SiO_2 nanospheres for synergistic catalysts in CO_2 reforming with methane reaction. *ACS Appl. Mater. Interfaces* **2022**, *14*, 23487–23495. [CrossRef]